Eur. J. Mineral., 35, 949–967, 2023
https://doi.org/10.5194/ejm-35-949-2023
© Author(s) 2023. This work is distributed under
the Creative Commons Attribution 4.0 License.

European Journal of Mineralogy
Open Access

Near-infrared signature of hydrothermal opal: a case study of Icelandic silica sinters

Maxime Pineau[1,2], **Boris Chauviré**[3,4], **and Benjamin Rondeau**[1]

[1]Nantes Université, Université d'Angers, Le Mans Université, CNRS, UMR 6112, Laboratoire de Planétologie et Géosciences, 44000 Nantes, France
[2]Laboratoire d'Astrophysique de Marseille, Aix-Marseille Université, UMR CNRS 7326, CNES, 13388 Marseille, France
[3]Université Grenoble-Alpes, Université Savoie Mont Blanc, CNRS, IRD, IFSTTAR, ISTerre, 38000 Grenoble, France
[4]GeoGems, 44350 Guérande, France

Correspondence: Maxime Pineau (maxime.pineau@lam.fr)

Received: 19 March 2023 – Revised: 6 September 2023 – Accepted: 12 September 2023 – Published: 13 November 2023

Abstract. Silica minerals constitute a main target to assess the origin of life or the possibility of its emergence. On Earth, ancient hydrothermal silica deposits have preserved the oldest forms of life. Beyond Earth, such silica-rich hydrothermal systems have been observed on Mars by orbital near-infrared (NIR) remote sensing and in situ rover exploration. This work investigates the variations of texture and NIR properties of opal with temperature, within a single geological context of hot springs. Silica sinters have been sampled in Icelandic hot-spring fields, in the Reykholt region, and at the Hveravellir site, with water temperature ranging from 14 to 101 °C. Variations in the NIR spectral features (concavity ratio criteria, CRC) vary with fluid temperature, lithofacies, and microtexture. Only high-temperature samples display high CRC values ($CRC_{5200} > 0.85$), but low CRC values ($CRC_{5200} < 0.75$) are measured for any temperature. Hence, temperature is not the only parameter controlling spectral properties of opal. Several other parameters such as the hydrodynamic context, the microbial activity, silica micro-textures, and porosity may also affect silica precipitation, the incorporation and speciation of water in it, and thus its NIR signature. The observations suggest a limitation in the use of NIR spectral features for the interpretation of the geological context of fossil opal on Earth or Mars: only opal with high CRC values can be inferred as being formed by hydrothermal activity. Low CRC values can be attributed to either low-temperature hydrothermal activity (< 50–60 °C) or to continental weathering.

Highlights.

- Low-temperature hydrothermal opals show near-infrared (NIR) properties similar to those of weathering opals.
- The variability of the NIR properties of Icelandic silica sinters is shown to be related to different conditions of formation, not only to temperature.
- Fluid temperature, hydrodynamics, microbial activity, and silica micro-textures may have complex influences on the NIR signature of hydrothermal silica.

1 Introduction

Opal ($SiO_2 \cdot nH_2O$) is an amorphous silica mineral with water content up to ∼ 18 wt % (Jones and Segnit, 1971; Day and Jones, 2008; Thomas et al., 2013; Chauviré and Thomas, 2020). It is a common alteration phase that forms in various geological contexts in close relationship with water–rock interactions in the near surface, mainly by continental weathering and hydrothermal activity. Since its detection on Mars by both orbital remote sensing (e.g., Milliken et al., 2008; Carter et al., 2023) and in situ rover observations (Squyres et al., 2008; Ruff et al., 2011; Morris et al., 2016), many authors have studied its potential to reconstruct the geological history

of water on Mars (e.g., Rice et al., 2013; Sun and Milliken, 2018; Pineau et al., 2020; Pan et al., 2021). Several studies demonstrate that the near-infrared (NIR) signatures of opal vary according to the formation process involved in terrestrial samples and to a lesser extent for martian occurrences (Chauviré et al., 2017a; Pineau et al., 2020; Pan et al., 2021). The interest of silica minerals in planetology is not limited to terrestrial planets, as silica particles have been detected in the hydrothermal jets ejected out of the South Pole of Enceladus (Saturn's moon), suggesting that water–rock interactions take place inside the icy moon (Hsu et al., 2015).

Moreover, opal is of key interest for astrobiological purposes. The oldest fossils on Earth are preserved in silica-rich ancient hydrothermal deposits, suggesting that the emergence of life could be related to hydrothermal energy (Djokic et al., 2017; Damer and Deamer, 2020). Opal is also recognized as an excellent preservative agent for organic matter and micro- to macrofossils (e.g., Barghoorn and Tyler, 1965; Rondeau et al., 2012; Chauviré et al., 2017b, 2020; Fox-Powell et al., 2018; Bell et al., 2019; Herrmann et al., 2019; Liesegang and Gee, 2020; Teece et al., 2020). Terrestrial hydrothermal zones, especially hot springs, geysers, fumaroles and marine black/white smokers, combine abundant concentrations of silica and life in close association (Kelley et al., 2002; Des Marais and Walter, 2019; Guido et al., 2019). Thereby, on any planetary body, current or past hydrothermal activity sites are priority targets for the search of past or present extraterrestrial life (Walter and Des Marais, 1993; Cady et al., 2018; Teece et al., 2020; Choblet et al., 2021). Some opaline silica deposits on Mars (e.g., Nili Patera) are suspected to be related to surface manifestations of hydrothermal activity, on the basis of their geomorphology and spectroscopic properties (Skok et al., 2010; Ruff et al., 2019; Pineau et al., 2020).

Silica formation in hot springs results from the cooling of hot water leading to the precipitation of opal-A, which can then mature into opal-CT, then chalcedony through early diagenesis processes (e.g., Kastner et al., 1977; Herdianita et al., 2000; Rodgers et al., 2004; Jones and Renaut, 2007; Lynne et al., 2007). It can precipitate in a large range of temperatures and exhibit very contrasting microstructures and textures, which are influenced by numerous biogenic and abiogenic parameters (e.g., Jones et al., 1997; Jones and Renaut, 2003a, b; Konhauser et al., 2004; Handley et al., 2005; Tobler et al., 2008; Boudreau and Lynne, 2012; Hamilton et al., 2019; Sriaporn et al., 2020; van den Heuvel et al., 2020). In vent areas with boiling springs and geysers, silica-rich deposits are defined as geyserite and associated with hot fluids ($T > 75\,^{\circ}C$; Walter, 1976; Campbell et al., 2015; Jones, 2021). The term silica sinter (or siliceous sinter) covers a wider range of silica deposition related to hot-spring activity (Campbell et al., 2015; Jones, 2021). The work by Chauviré et al. (2017a) suggests that hydrothermal opal-A (i.e., silica sinter, including geyserite) has a singular spectral signature that differentiates them from surface continental weathering opals. However, this hydrothermal versus continental weathering distinction is based on a thermal threshold where opals formed at $T > 50\,^{\circ}C$ are considered hydrothermal in origin. This definition does not consider samples formed in a hot-spring context at lower, near-ambient temperatures ($T < 50\,^{\circ}C$). The aim of this study is therefore to verify whether all hydrothermal silica formed around hot springs exhibit spectral signature consistent with a hydrothermal origin. The study documents the NIR properties of silica sinters deposited at temperatures ranging from ambient (14 °C) to 100 °C and showing a large variety of microtextures. In this sense, the present study brings constraints on the use of NIR properties as a tool for interpreting the geological origin of fossil silica sinters on Earth and Mars.

2 Materials and methods

2.1 Sampling sites and fieldwork

A total of 94 silica sinter and geyserite samples were collected in a series of hot springs areas in Iceland during a field trip in August 2018 (Fig. 1), under supervision of the Matís organization, in the frame of an EuroPlanet research program. A total of 17 silica samples were removed due to mixing with other hydrated mineral phases (see Results section). The list of the remaining 77 samples and their corresponding temperatures is given in Supplement S1. Hveravellir (samples noted HVR-; 64°51′55″ N, 19°33′24″ W), in central Iceland, is a field with several hot springs covering an area about 150×200 m (Fig. 1, inset). All vents of the Hveravellir field, including both active and fossil springs, fumaroles and mud pools, were mapped during the field investigation (map modified after Torfason, 1997, Fig. 2). The remaining samples come from a small area around Reykholt, western Iceland, about 25 km northeast of Borgarnes. Most of these come from small, single, low-flow hot springs, labeled after the names of the closest localities, generally consisting of a few houses: Hurðarbak (HDK-; 64°41′18″ N, 21°24′10″ W); Haegindi (HAE-; 64°39′17″ N, 21°17′1″ W); an unnamed pumping plant that was named POM- (64°39′11″ N, 21°21′35″ W) near Logaland; and Deildartunguhver, the highest-flow hot spring in Europe, where the Krauma company manages geothermal baths (KRO-; 64°39′46″ N, 21°24′40″ W).

All sites were chosen for their silica precipitation products. Hot-spring fluids emerge from the vent at high temperatures and cool down when flowing away. Silica deposits were sampled at places selected for temperatures in the largest range as possible for each location. For each sample, both water pH and temperature were measured at the exact sampling place. pH was established using pH paper as the electronic pH meter encountered operating difficulties due to local climate. Observed pH always fell in the 8.0–8.5 range, and thus it will be considered nearly constant hereafter. In situ fluids

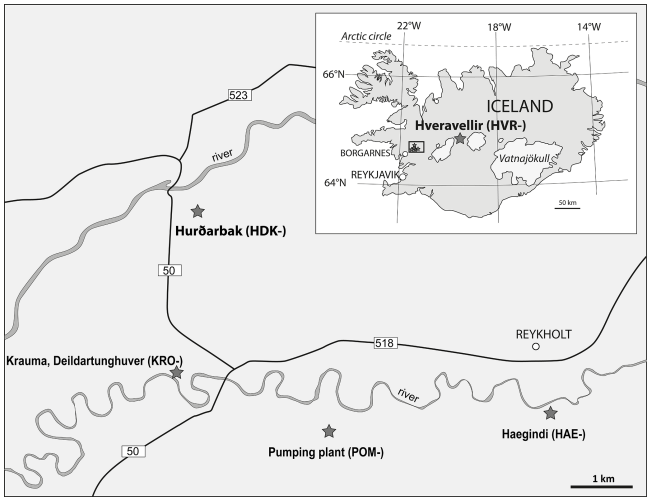

Figure 1. Location of sampling sites, hydrothermal vents in Iceland: Hveravellir in central Iceland (inset) and the Borgarnes–Reykholt area in western Iceland (main map; black rectangle in inset). A detailed map (modified from Torfason, 1997) of the Hveravellir geothermal site is available in Fig. 2.

temperatures were measured using an electronic laboratory thermometer for several tens of seconds to wait for a stable averaged temperature. Fluid temperatures occur in the range 14–101 °C. Waters colder than 14 °C proved not to precipitate silica anymore in a significative manner. The variability of temperature was tested in each sampling site by measuring it at different points about 10 cm around the sample, and it proved to be less than 1 °C. The measured temperatures are hence considered representative of the place of silica formation.

2.2 Sample preparation and lithofacies classification

Each sample was split using a diamond saw into several parts for distinct preparation. Sawing was carried out without water or oil, to not modify the hydrated state of the samples or add organic compounds. To avoid heating up of the sample during sawing, which can increase dehydration of the material, the saw speed was set to a minimum. One part was consolidated into epoxy and then prepared as a polished section for texture observation under optical and electronic microscopes. Other parts were dedicated to spectral investigations and X-ray diffraction analyses and prepared without epoxy to avoid artifacts due to preparation. In order to check for possible variations within a single sample, each sample was sub-sampled by scraping off with a scalpel some fragments of the top layer, the bottom layer, and when appropriate, the internal zone. The obtained fragments were finely powdered using an agate mortar for XRD and NIR analysis.

According to their in situ context of occurrence, macroscopic morphology/texture and microscopic features under the optical microscope, the samples were classified into seven distinct lithofacies using the classification of Hamilton et al. (2019): (i) palisade fabrics, (ii) clotted fabrics, (iii) finely laminated sinter, (iv) streamer fabrics, (v) geyserite (spicular/nodular), (vi) geyser egg and (vii) radiating macrobotryoidal geyserite. The characteristics of each lithofacies are provided in Table 1. Some examples for each lithofacies are illustrated in Figs. 3, 4, and 5.

2.3 Analytical methods

Optical microscope observations were done at the Laboratoire de Planétologie et Géosciences (UMR-CNRS-6112, Nantes Université, France) using a Keyence VHX2000 digital microscope allowing magnification from 20× to 1000×. This instrument was mainly used to produce 2D maps of the polished sections. These images were used as guide maps for microscopic observations at smaller scales using a scanning electron microscope. The scanning electron microscopy (SEM) micrographs were recorded at the Institut des Matériaux Jean Rouxel de Nantes (IMN; UMR-CNRS-6502, Nantes Université, France) using a JEOL JSM 7600F microscope operating at 10 kV. Samples were coated with platinum. Carbon coating was avoided to observe and measure carbon abundance in the samples. Both Raman spectroscopy and X-ray diffraction (XRD) were used to determine the type of opal and select only mineralogically pure samples.

Raman spectra, measured at the Laboratoire de Planétologie et Géosciences, were acquired using a LabRAM Jobin–Yvon Raman spectrometer equipped with an Ar laser emitting at 514 nm (50 mW power) combined with a microscope with a 50× objective; a 1200 lines per millimeter grating providing a 2 cm^{-1} resolution was used. Each spectrum is an accumulation of 5 to 30 scans with acquisition times about 5 to 60 s per scan.

X-ray diffraction (XRD) patterns were collected at the IMN at room temperature on a Bruker D8 diffractometer using monochromatic Cu K-L3 ($\lambda = 1.540598$ Å) X-rays, a 1D Si detector, and a Ge (111) monochromator, in the Bragg–Brentano ($\theta/2\theta$) configuration. Diffractograms were acquired from 4 to 70° 2θ with a step of 0.012° 2θ and 1.012 s counting time per step, for a total acquisition time of 5567 s (∼90 min).

Reflectance near-infrared (NIR) acquisitions were conducted at the Institut de Chimie des Milieux et des Matériaux de Poitiers (IC2MP, UMR-CNRS 7282, Université de Poitiers, France). NIR spectra were acquired using a Thermo Fisher Scientific Nicolet 6700 FT-IR Spectrometer equipped with a Thermo Scientific Near-IR Integrating Sphere with an internal InGaAs detector, an internal gold reference material and a tungsten–halogen white-light source. All the internal setup of the integrating sphere was atmospherically controlled by a constant flow of dry air. Sample powders were deposited onto the sapphire window of the integrating sphere; powders were thus in contact with ambient air.

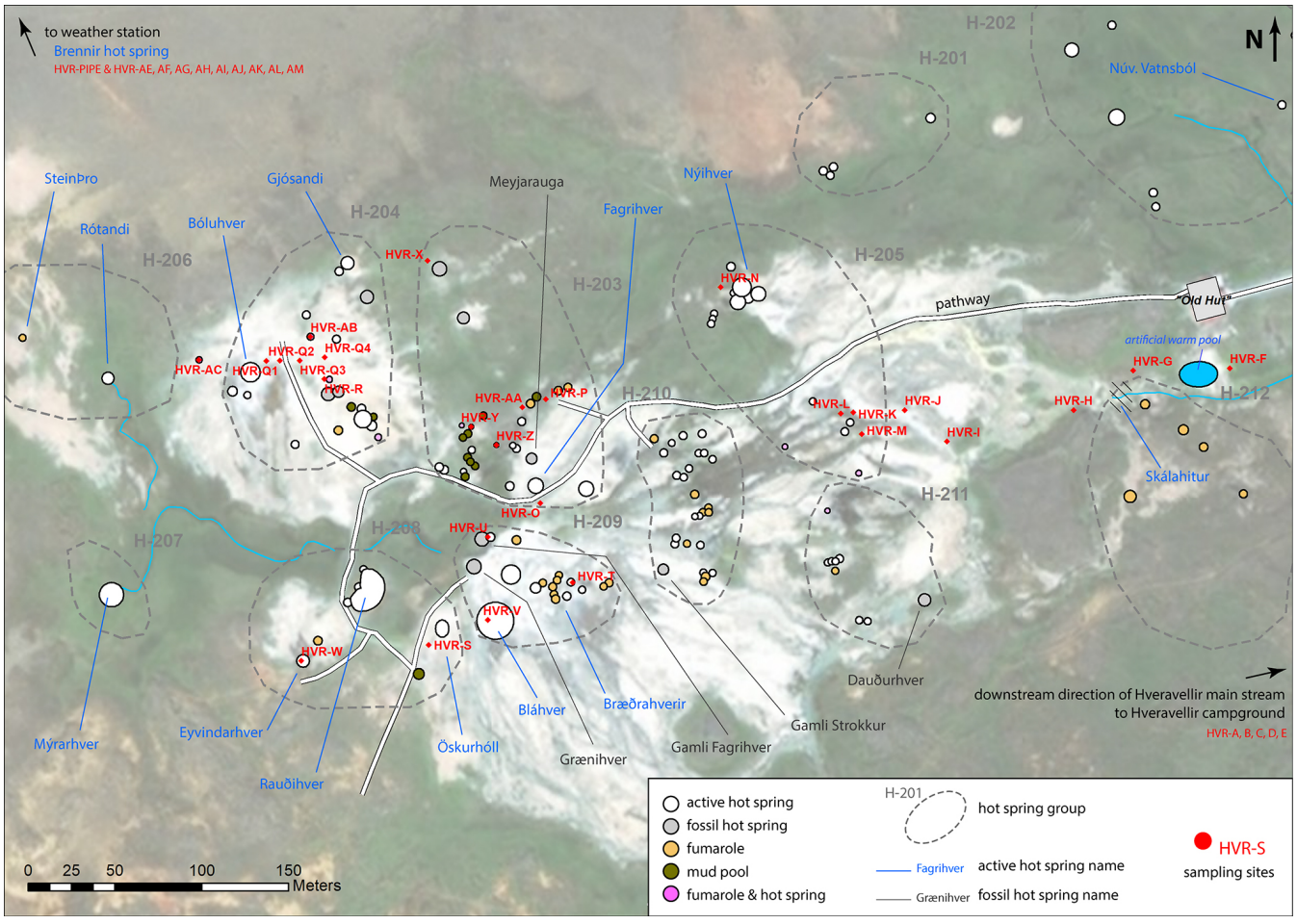

Figure 2. Detailed map of the Hveravellir geothermal site with sampling locations. The hot-spring groups shown on the map in dashed lines and annotated with the nomenclature "H-xxx" are from Torfason (1997).

Each spectrum is an accumulation of 100 scans with a spectral resolution of 2 cm^{-1} in the 4000 to 10 000 cm^{-1} spectral range (1.0 to 2.5 µm). All NIR spectra are available in Supplement S2.

2.4 Spectral criteria

Silica sinters NIR spectra exhibit several absorptions related to water (H_2O) and silanol (SiOH); both can be free or hydrogen-bonded (Table 2). These absorptions vary in position and shape according to the type of silica, crystallinity, water content, and geological formation pathways (Anderson and Wickersheim, 1964; Langer and Florke, 1974; Rice et al., 2013; Christy, 2011; Boboň et al., 2011; Chauviré et al., 2017a, 2021; Sun and Milliken, 2018). The following NIR spectral criteria were used to assess the type of silica and to confront the geological origin (calculation procedures are detailed in Supplement S3):

– The minimum position of the 7000 cm^{-1} absorption is the position of minimum of reflectance of the 7000 cm^{-1} absorption band, which is an indicator of the crystallinity and type of silica. As stated in Chauviré et al. (2017a), Sun and Milliken (2018), and Pineau et al. (2020), silica samples with lower minima position are composed of amorphous silica (opal-A). Samples with higher minima positions are composed of more crystalline silica (opal-CT or chalcedony).

– $BDR_{5235/5100}$ (for "band depth ratio of the 5235 and 5100 cm^{-1} absorptions") corresponds to the $BDR_{1.91/1.96}$ of Rice et al. (2013), which quantifies the shape of the 5200 cm^{-1} absorption (1.9 µm).

– $BDR_{4525/4425}$ (for "band depth ratio of the 4525 and 4425 cm^{-1} absorptions") corresponds to the $BDR_{2.26/2.21}$ of Sun and Milliken (2018), which quantifies the shape of the 4500 cm^{-1} absorption (2.2 µm).

– CRC_{5200} and CRC_{7000} (for "concavity ratio criterion of the 5200 cm^{-1}" and "7000 cm^{-1}", respectively) was defined by Chauviré et al. (2017a); they permit the quantification of the shapes of the high-frequency sides of

Table 1. Description of the lithofacies identified according to the different in situ contexts and macroscopic observations following Hamilton et al. (2019). Fig. denotes the figure where the lithofacies are illustrated.

Lithofacies	Description	Fig.
Palisade fabrics	Samples with silica layers incorporating silicified microbial mats, plant debris and some micrometric detrital grains. Samples located near/around streams and aprons. Low-temperature samples ($10\,°C < T < 35\,°C$).	3a
Clotted fabrics	Samples with silica that can be slightly laminated but generally without peculiar structure. Samples present a "fragile" and "powdery" character with a "cottony", "snowy", "wooly" or "rounded rod-shaped" appearance. Samples located away from vents. Low- to mid-temperature samples ($10\,°C < T < 65\,°C$).	3b
Finely laminated sinter	Samples exhibiting more or less wavy laminated silica layers with low porosity density and few radial structures. Common samples across all hot-spring sites, from vents to aprons. Large range of temperatures for these samples ($25\,°C < T < 110\,°C$).	4a, b
Streamer fabrics	Laminated sinter exhibiting a great density of inframicrometric-to-micrometric pores between the silica layers. Common samples across all hot-spring sites, from vents to aprons. Large range of temperatures for these samples ($25\,°C < T < 110\,°C$).	4c
Geyserite (spicular/nodular)	Samples exhibiting micrometric spicular/nodular/columnar surface growths. Samples located in or near hot-spring vent pools, sometimes within the "splash" zones. High-temperature samples ($T > 90\,°C$).	5a
Geyser egg	Hand-sized pebble shape, ovoid samples with various surface and internal structures; the term "geyser egg" is due to the overall macroscopic morphology. Samples located near hot-spring vents within shallow basins located in the "splash" zones. Geyser eggs usually develop in shallow pools. Mid- to high-temperature samples ($T > 65\,°C$).	5b
Radiating macrobotryoidal geyserite	Samples exhibiting surface growths with domal, hummocky or knobby morphologies. Samples located near the hot-spring vents area. Mid- to high-temperature samples ($T > 60\,°C$).	5c

the 5200 and 7000 cm^{-1} absorptions. They permit the assessment of the geological origin: hydrothermal versus low-temperature weathering opal. Thresholds and uncertainty ranges between hydrothermal and weathering fields are refined from Chauviré et al. (2017a) in the light of the new data presented in this paper; see Results section and Supplement. In their paper, the boundaries between the weathering and hydrothermal fields are based on a thermal definition. The hydrothermal field refers to $T > 50\,°C$, whereas the weathering field refers to $T < 50\,°C$ (Pirajno, 2009). However, since the present samples come from hydrothermal active areas only, the weathering field in the CRC diagrams should be understood here as low-temperature hydrothermal activity ($T < 50$–$60\,°C$) and the hydrothermal field as mid- to high-temperature hydrothermal activity ($T > 50$–$60\,°C$).

3 Results

3.1 Microscopic texture variations and biological features

Under the scanning electron microscopic (SEM), a large variety of textures are regularly observed in all samples; these textures are not specific to any lithofacies. The samples commonly show well-cemented to uncemented silica spheres, typical of opal-A. This contrasts with opal-CT, which is typically composed of more complex structures such as lepispheres (Lynne et al., 2005, 2007; Jones and Renaut, 2007; Gaillou et al., 2008). Silica spheres show diameters ranging from less than 100 nm to more than 20 µm. Textural variations are observed from one sample to another. For some samples, such variations are observed at the scale of hundreds of micrometers, making them very heterogenous at the microscale (Fig. 6).

The most commonly observed silica microtextures are the following: (i) uncemented, with silica spheres consisting of perfectly spherical silica without cement in between, their diameter being not sorted: the spheres are packed with no order (Fig. 6c), (ii) spheres partially cemented, with some space remaining between the spheres (Fig. 6b), or (iii) well

Table 2. Near-infrared absorptions of molecular water (H_2O_{mol}), silanol groups (SiOH), and hydroxyls (OH) in amorphous hydrated silica (opal) after Anderson and Wickersheim (1964), Langer and Florke (1974), and Rice et al. (2013). Vibration modes: δ_{SiOH} denotes SiOH bending in plane, υ_{OH} the OH stretching, υ_1 the symmetric stretching, υ_2 symmetric bending, and υ_3 antisymmetric stretching.

Band position in cm^{-1} (µm equivalent)	Band attribution	Vibration mode
4420 (2.26)	Silanol SiOH (H-bonded) stretching + siloxane Si–O–Si bending	$\delta_{SiOH} + \upsilon_{OH}$
4500 (2.21)	Silanol SiOH (isolated) stretching + siloxane Si–O–Si bending	$\delta_{SiOH} + \upsilon_{OH}$
5100 (1.96)	Combination of OH stretching and bending in water molecules (H-bonded)	$\upsilon_2 + \upsilon_3$
5250 (1.91)	Combination of OH stretching and bending in water molecules (isolated)	$\upsilon_2 + \upsilon_3$
6850 (1.46)	Combination of OH stretching and bending in water molecules	$2\upsilon_2 + \upsilon_3$
7090 (1.41)	Overtone of OH stretching in silanols SiOH	$2\upsilon_{OH}$
8695 (1.15)	Combination of OH stretching in water molecules	$\upsilon_1 + \upsilon_2 + \upsilon_3$

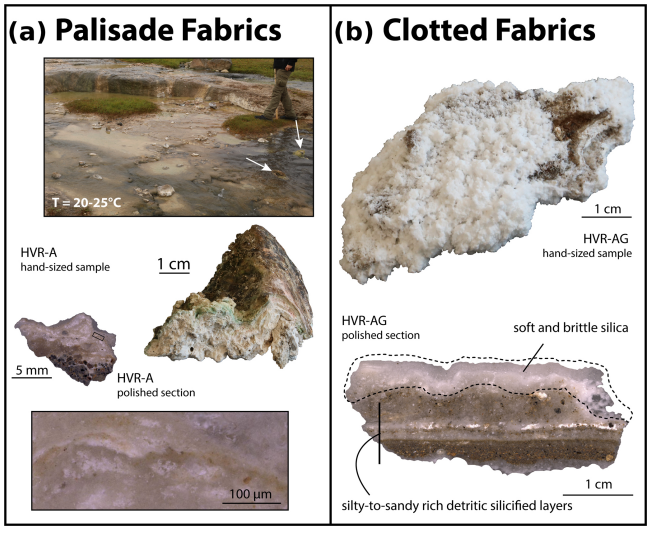

Figure 3. Examples of **(a)** palisade fabrics lithofacies environment and samples. Top: main water discharge stream at the Hveravellir hot-spring site. White arrows indicate mounds of silicified biological material. Below: hand-sized sample (right) and the corresponding polished section (left). The inset shows a zoom over an area with a mixture of microbial mats (greenish to brown parts) and silica (whitish parts). **(b)** Clotted fabrics lithofacies hand-sized sample (top) and the corresponding polished section (below) showing the silica precipitation over silicified silty-to-sandy rich detrital materials.

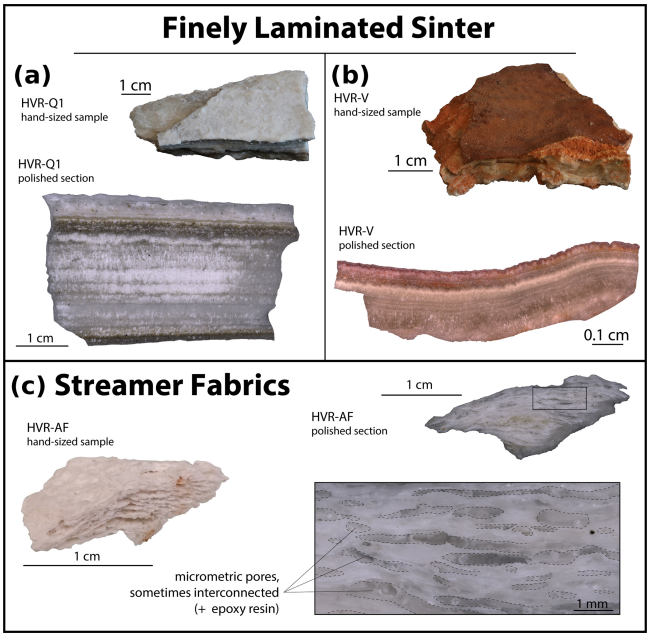

Figure 4. Examples of **(a–b)** Finely laminated sinter hand-sized samples (top) and the corresponding polished sections (below). Samples show obvious silica coherent platelets with on occasion fibrous textures. **(c)** Streamer fabrics lithofacies hand-sized sample (left) and the corresponding polished section (right). The inset shows a zoom over wavy-laminated silica layers exhibiting millimetric pores (outlined in dashed lines) that are sometimes interconnected.

cemented, the texture appearing massive and homogeneous (top layer in Fig. 6a). Silica spheres can arrange themselves to form elongated, irregular, ramified rods with rounded ends, up to 100 µm long (Fig. 6d). Silica can also form sharp ended shards, elongated or triangular, also up to 100 µm long (Fig. 6e). The diverse cementation degrees and textures imply that the porosity (interconnected or not) can be described in two ways: (i) as holes, cracks, and fractures in large and massive cemented silica areas and (ii) as inter-particles space between the spheres.

Diverse microbiological features are also present (Fig. 7). Most of them consist of thin laminae of silicified microbial mats, sometimes combined with alveolar biologic organic matter (Fig. 7a). Some silicified diatom fossils are also observed (Fig. 7b, c), as well as the presence of more complex biological structures probably derived from silicified plant fragments (Fig. 7c) or microbial filaments communities (Fig. 7d). In most cases, the presence of both silicified and unsilicified microbiological features is associated with the presence of well-cemented silica or to finely layered silica laminae, never to uncemented silica spheres.

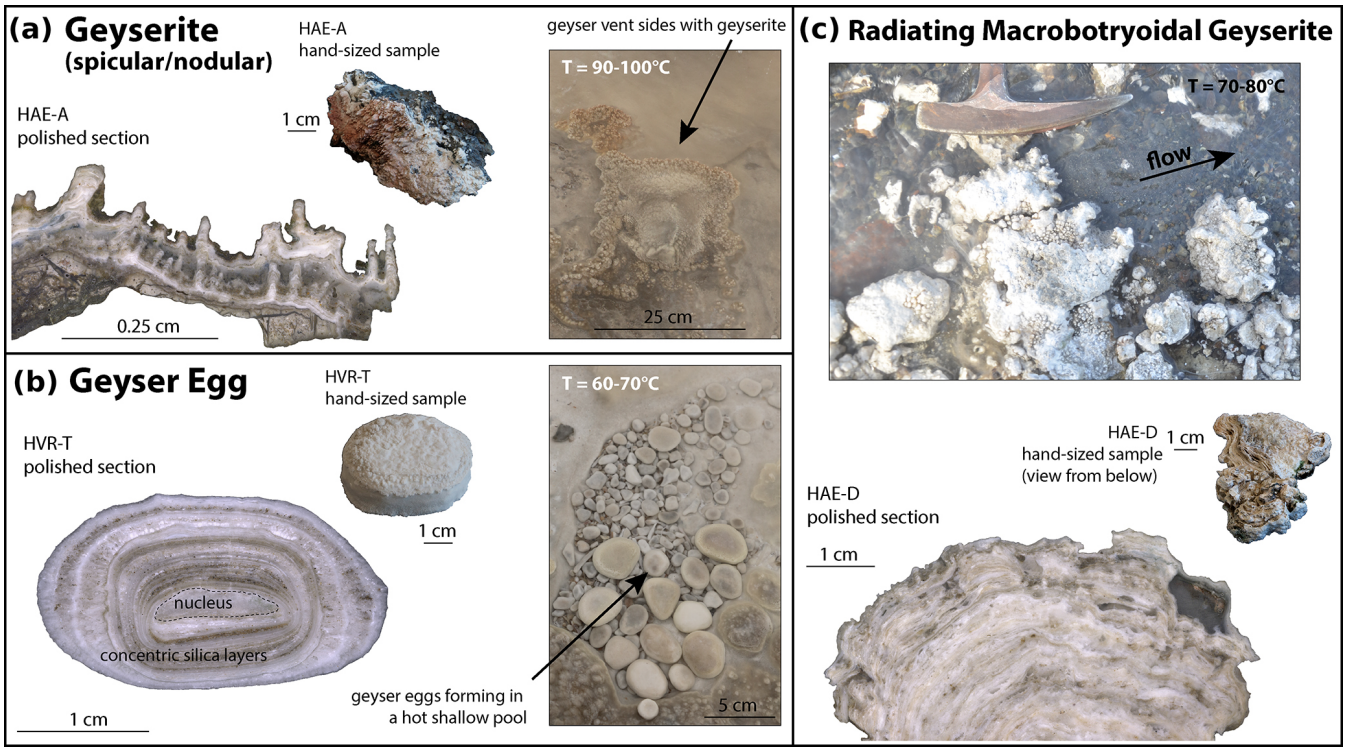

Figure 5. Examples of high-temperature geothermal contexts and corresponding lithofacies. **(a)** Geyserite lithofacies. Left: geyserite hand-sized sample and the corresponding polished section. Spicular silica in the macroscopic sample is shown to be formed of narrow columnar silica at the subcentimetric scale. Right: the Bræðrahverir hot-spring active vent. The edges of the active bubbling pool are composed of geyserite precipitations. **(b)** Geyser egg lithofacies. Left: example of a hand-sized sample and the corresponding polished section. Geyser eggs are made of concentric silica layer with possible fibrous and detrital textures around a core nucleus that can be siliceous or basaltic in nature. Right: geyser eggs "nest" in a shallow pool located in the "splash" activity area. **(c)** Radiating macrobotryoidal geyserite lithofacies. Top: picture of the near-vent discharge area of the Haegindi hot spring showing the presence of botryoidal geyserite fragments. Below: a hand-sized sample and the corresponding polished section.

3.2 Silica sinters mineralogy

The XRD diffractograms of all samples are dominated by a broad diffraction band centered at about 22°2θ (Fig. 8), typical of opal-A (Jones and Segnit, 1971). However, several samples show additional sharp XRD peaks and/or Raman peaks, indicative of phase mixture. This can induce misinterpretation in the NIR data if these additional phases are hydrated (gypsum for example). Therefore, the 17 samples exhibiting mixture were discarded, to conduct NIR measurements on spectrally pure opal. The remaining samples showed on occasion additional anhydrous phases (so devoid of water-related IR bands) such as plagioclase, native sulfur, and calcite (see Fig. 8).

The Raman spectra of the samples are all dominated by a broad band centered at about 420 cm^{-1} (Fig. 9), also indicative of opal-A (Smallwood et al., 1997; Ostrooumov et al., 1999). The amorphous nature of the silica is further indicated by the presence of a Raman band near 480 cm^{-1}, referred to as the D1-band, indicative of defects in the Si–O–Si ring structures (Galeener, 1982a, b; Phillips, 1984). A few samples that also show a weak Raman signal of additional phases, such as anatase or gypsum (Fig. 9), are kept in the dataset as these accessory phases are not detected by XRD nor NIR (see for example sample HVR-B in Figs. 8 and 9).

3.3 NIR and spectral criteria results

Typical NIR spectra for each lithofacies are shown in Fig. 10. The results of the spectral criteria for each sample are all available in Supplement S2. The samples from a given lithofacies share similar spectral characteristics, but these differ from other lithofacies. Hence, the mean values (with standard deviation) for each lithofacies are given in Table 3, and some are plotted in Fig. 11.

Among all samples, the reflectance minima of the 7000 cm^{-1} absorption range from 7043 to 7104 cm^{-1} (1.407 to 1.419 µm). This falls in the field of opal-A considering the values of Chauviré et al. (2017a) and Sun and Milliken (2018). Two main clusters of values can be drawn out: the lowest mean values are those of the geyserite and radiating macrobotryoidal geyserite lithofacies, with mean values

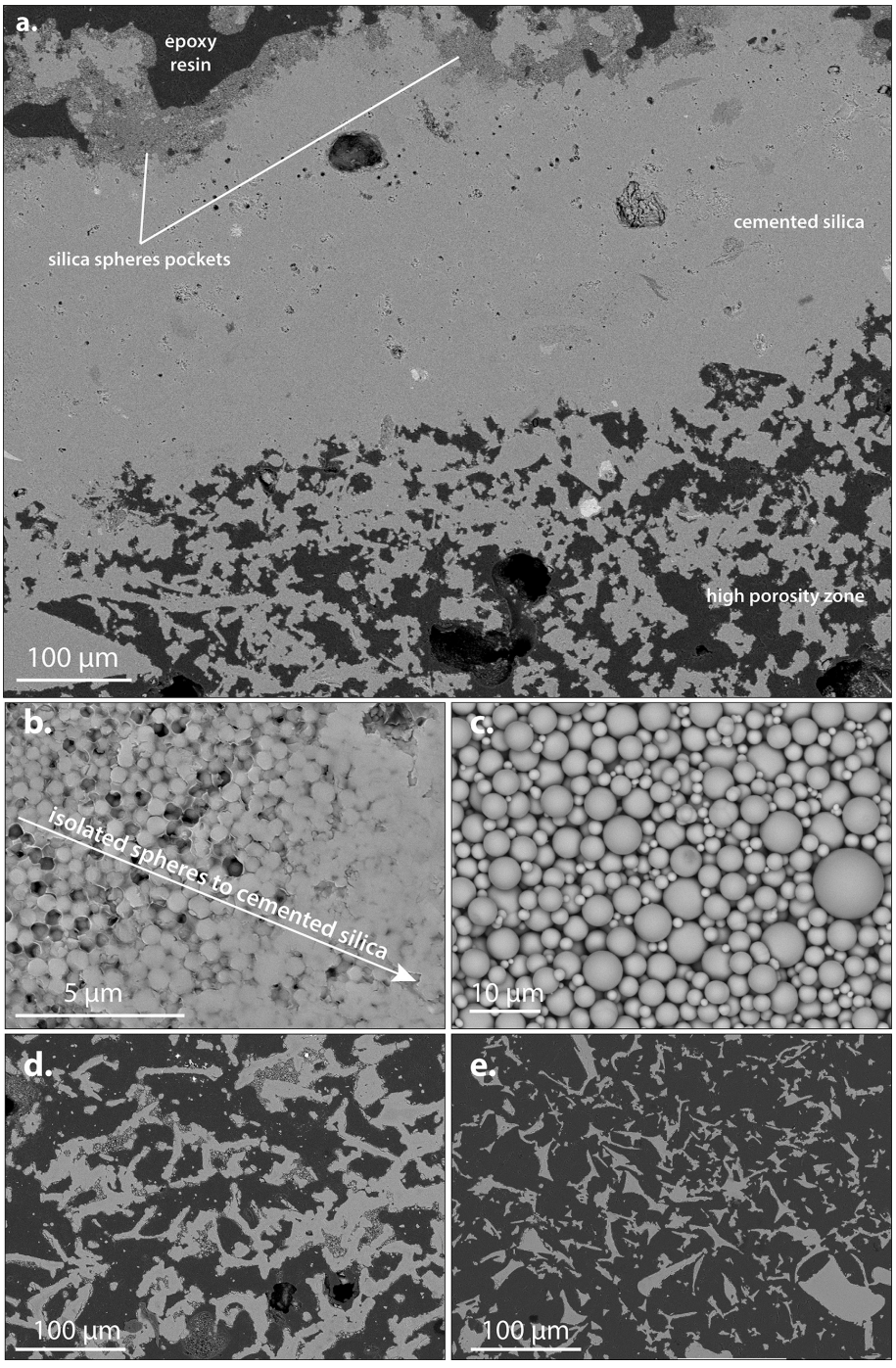

Figure 6. Electron microscopy images (backscattered electrons) illustrating the diversity of textures and cementation degrees of silica sinter samples. **(a)** Large-scale view of a silica sinter sample showing two main levels. Top part: layer of well-cemented silica topped with a thin layer composed of uncemented silica sphere pockets (zoomed in **c**), with an abrupt to progressive transition (zoomed in **b**). Bottom part: large, porous layer composed of a mixture of rounded rod-shaped silica (zoomed in **d**) and shard-shaped silica textures (zoomed in **e**).

of 7069 and 7071 cm^{-1} respectively (1.415 and 1.414 µm). The remaining five lithofacies show mean values higher than 7090 cm^{-1} (below 1.410 µm).

Among all samples, the band–depth ratio $BDR_{5235/5100}$ values range from 1.27 to 2.07. The mean values by lithofacies range from 1.42 to 1.79. Again, the values are split into two main clusters: (i) $BDR_{5235/5100} < 1.60$ for the geyserite and radiating macrobotryoidal geyserite lithofacies (1.42, and 1.44 respectively) and (ii) the other lithofacies with values > 1.60 ranging from 1.62 to 1.79.

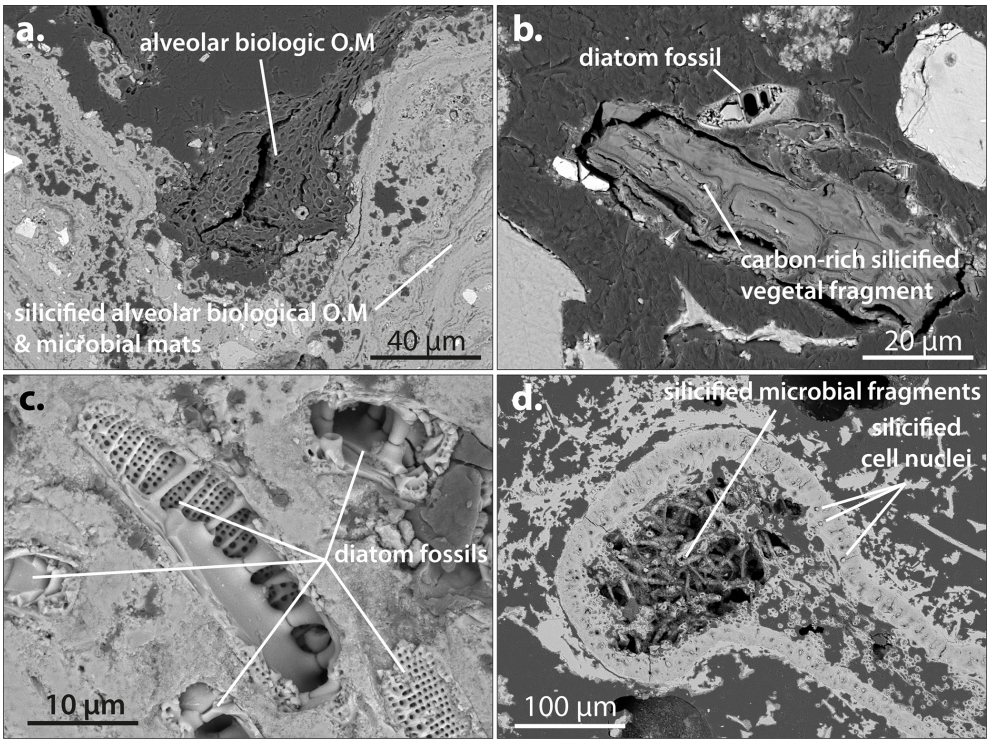

Figure 7. Electron microscopy images (backscattered electrons) showing diverse examples of partially silicified microorganisms in silica sinter. **(a)** Silicified alveolar biologic organic matter with silicified microbial mats covered by unsilicified alveolar biologic organic matter (OM). **(b)** Carbon-rich silicified vegetal organism and neighboring diatom skeleton. **(c)** Numerous diatom skeletons trapped in the silica sinter matrix. **(d)** Complex silicified biologic organism with silicified microbial filaments. Note the cell nuclei that have been silicified and replaced by large silica spheres.

Table 3. Mean near-infrared spectral characteristics of each lithofacies. See text for the signification of the abbreviations. For each mean value, the standard deviation is given in brackets. n: number of powder samples.

Lithofacies	7000 cm^{-1} band position	$BDR_{5235/5100}$	$BDR_{4525/4425}$	CRC_{7000}	CRC_{5200}	T °C
Palisade fabrics ($n = 7$)	7090.4 (0.9)	1.7 (0.09)	1.2 (0.07)	0.82 (0.07)	0.77 (0.05)	22.9 (5.2)
Clotted fabrics ($n = 15$)	7093.7 (3.4)	1.7 (0.07)	1.1 (0.08)	0.76 (0.05)	0.74 (0.04)	29.2 (13.7)
Finely laminated sinter ($n = 12$)	7093.9 (9.3)	1.7 (0.16)	1.0 (0.11)	0.79 (0.11)	0.75 (0.09)	72.3 (21.2)
Streamer fabrics ($n = 13$)	7089.8 (13.2)	1.6 (0.20)	1.0 (0.14)	0.84 (0.15)	0.80 (0.12)	75.2 (26.8)
Geyserite ($n = 9$)	7068.8 (16.8)	1.4 (0.10)	0.9 (0.15)	1.00 (0.09)	0.92 (0.07)	97.4 (4.3)
Geyser egg ($n = 11$)	7097.4 (5.6)	1.8 (0.14)	1.0 (0.08)	0.72 (0.06)	0.70 (0.06)	91.4 (11.8)
Radiating macrobotryoidal Geyserite ($n = 10$)	7071.5 (8.2)	1.4 (0.05)	0.9 (0.10)	1.00 (0.05)	0.91 (0.03)	85.9 (10.5)

Among all samples, the $BDR_{4525/4425}$ values range from 0.67 to 1.32. The mean values by lithofacies range from 0.91 to 1.18. Here again, two main clusters appear, but they differ from those defined by the three previous criteria: palisade fabrics and clotted fabrics lithofacies show $BDR_{4525/4425} > 1.10$ (1.18 and 1.14), when the remaining five lithofacies show values < 1.05, ranging from 0.91 to 1.02.

Among the full dataset, the CRC applied to both absorption bands (7000 and 5200 cm^{-1}) ranges from 0.60 to 1.13 (7000 cm^{-1} band) and 0.58 to 1.03 (5200 cm^{-1} band). Two main clusters according to lithofacies clearly appear: geyserite and radiating macrobotryoidal geyserite are the lithofacies that exhibit highest CRC values ($CRC_{7000} > 0.95$; $CRC_{5200} > 0.85$), whereas the remaining five lithofacies show lower CRC values (CRC_{7000} from 0.72 to 0.84; CRC_{5200} from 0.70 to 0.80).

3.4 Criteria combination diagrams

The comparison between spectral parameters can help to classify the type of silica and check for NIR properties variations within a single geological context. Criteria comparisons are presented in Fig. 11, where the values used for Fig. 11a

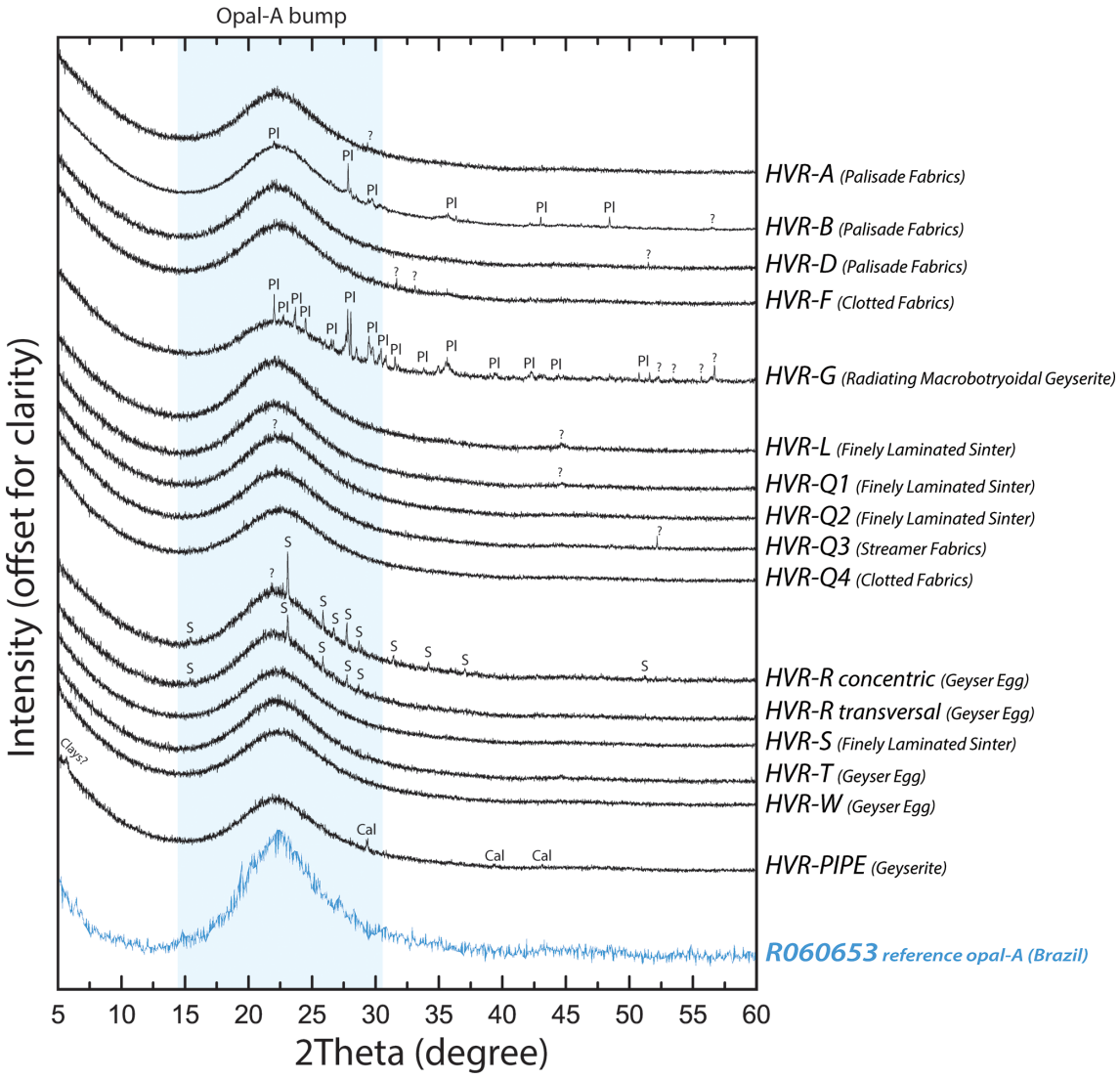

Figure 8. Selected XRD diagrams of representative Icelandic silica sinter samples. All are dominated by a broad diffraction band centered at about 22°2θ (a reference XRD diagram from the RRUFF database is given for comparison: https://rruff.info/R060653, last access: 26 June 2023). Additional phases: Pl – plagioclase; Cal – calcite; S – native sulfur.

and b are those of Supplement S2 (individual samples), and those of Fig. 11c and d are those of Table 3 (mean values of the seven lithofacies). Figure 11a is the plot of the CRC_{5200} versus the CRC_{7000}. The hydrothermal and weathering fields are indicated based on Chauviré et al. (2017a). All the individual samples data points follow a linear correlation with a high correlation coefficient: $R^2 > 0.98$. This high R^2 value shows that the two CRC calculations are consistent with each other. Therefore, we chose to further use the CRC_{5200} only, as it provides the most precise information (Chauviré et al., 2017a).

The possible relationship between temperature and CRC values is checked by plotting both parameters in Fig. 11b. No definitive and obvious relationship can be observed between these two, but some notable features can be drawn out. At low to mid-temperatures ($T < 60\,°C$), nearly all CRC measurements fall within the field of continental weathering. This concerns mainly two lithofacies: palisade fabrics and clotted fabrics. At high temperatures ($T > 80\,°C$), the geyserite and radiating macrobotryoidal geyserite lithofacies clearly fall within the hydrothermal field, with CRC values all above 0.85. However, the geyser eggs display among the lowest CRC values despite a high temperature. In the same way, the finely laminated sinter and streamer fabrics lithofacies formed at various temperatures (45 to 100 °C) and display CRC values in a large range ($CRC_{5200} = 0.58$ to 1.02, $CRC_{7000} = 0.60$ to 1.12) but with no clear correlations between CRC and temperature.

The diagrams in Fig. 11c and d combine the band–depth ratios $BDR_{5235/5100}$ and $BDR_{4525/4425}$ with the minimum of

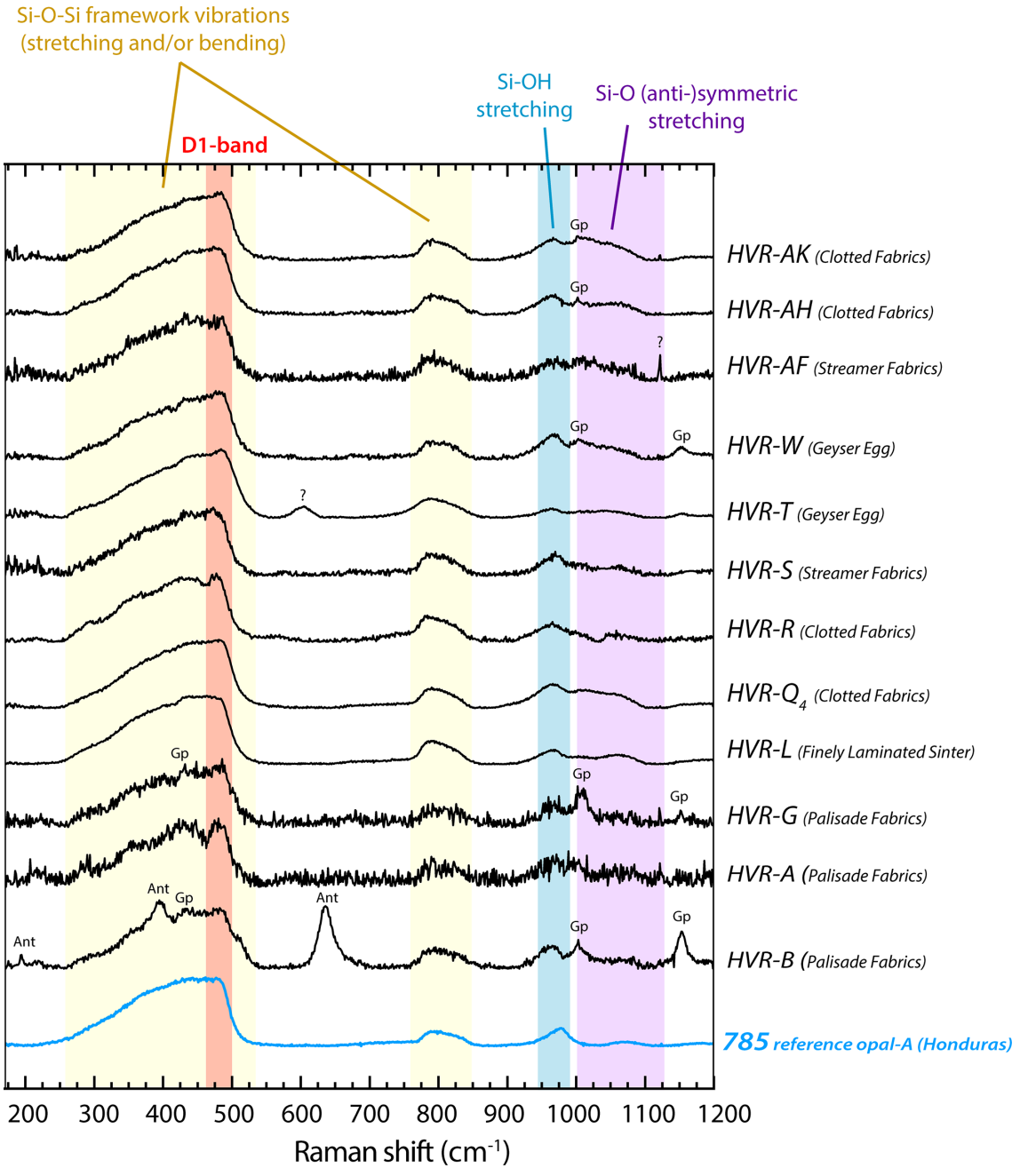

Figure 9. Examples of Raman spectra of Icelandic silica sinter samples. All spectra are dominated by the features typical of opal-A (a reference spectrum is given for comparison; Chauviré et al., 2017). Other peaks that show the presence of other minor phases are also indicated (Ant for anatase, Gp for gypsum).

reflectance of the 7000 cm^{-1} absorption band, respectively. In Fig. 11c, all the lithofacies mean values fall in the opal and sinter field defined by Rice et al. (2013). As described in the subsection above, the dataset is divided into two main clusters. Figure 11d shows that all samples fall in the overlap between opal-A and more crystalline silica (grouping opal-CT, opal-C, and chalcedony) defined by Sun and Milliken (2018).

4 Discussion

4.1 Structural characterization

The samples are composed of opal-A as shown by conventional XRD and Raman spectroscopy results. NIR properties (band depth ratios, band position, and CRC values defined in earlier studies, Rice et al., 2013; Chauviré et al., 2017a; Sun

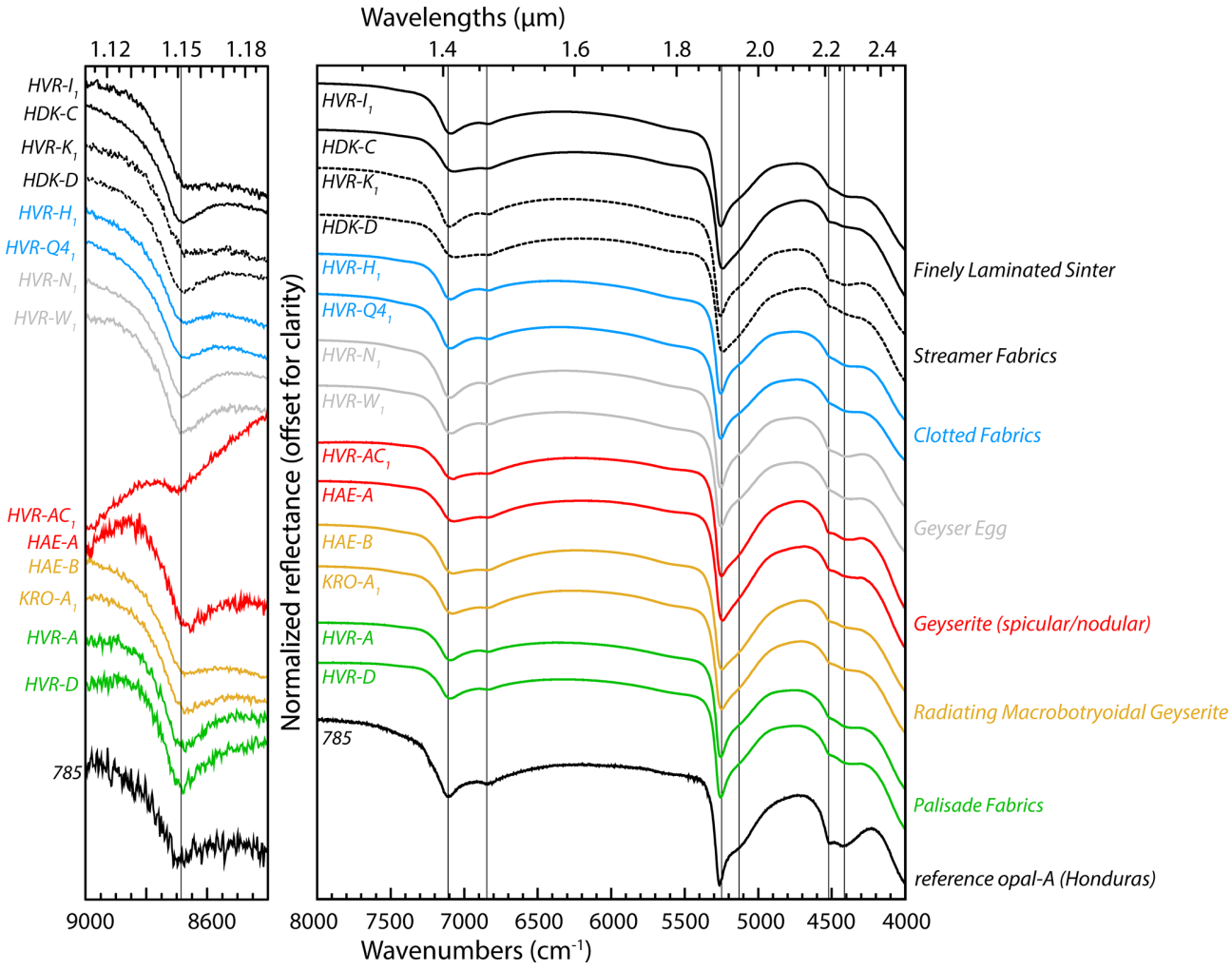

Figure 10. Examples of near-infrared spectra of Icelandic silica sinter powdered samples. The spectra are colored according to their lithofacies class. All spectra are dominated by the features typical of opal-A (a reference spectrum is given for comparison; Chauviré et al., 2017). The main absorptions bands of hydrated silica are indicated as vertical lines (their corresponding molecular vibrations are detailed in Table 2). The positive spectral slope in the 9000–8400 cm^{-1} (1.12–1.18 µm) range for the HVR-AC_1 sample is caused by non-hydrous Fe oxides.

and Milliken, 2018) are also all indicative of opal-A, which confirms the robustness of these infrared criteria.

The investigation by electron microscopy reveals a great variability of textures, including entirely free silica spheres, massive silica, laminations, stromatolitic-like features, etc. All these textures provide similar XRD patterns and Raman spectra, indicating that the (micro-)texture does not affect the degree of crystallinity of opal. However, they affect the NIR properties, as revealed by the variability of the spectral criteria measured in this study.

4.2 Parameters influencing NIR properties

4.2.1 Lithofacies and temperature

The spectral investigation indicates that different samples within a given lithofacies show similar NIR properties in terms of band minima and band shapes. Similarly, the temperature range associated with each lithofacies is generally narrow (on the order of 10 to 30 °C), except for the streamer fabrics and finely laminated sinter (temperature range of 42 and 53 °C respectively). Silica deposition into platy-to-wavy laminae is the most classical formation mechanism of silica sinter (e.g., Hamilton et al., 2019). Laminated sinters form all along a hot-spring profile (from the vent to the most distal precipitation), from high (> 80 °C) to low temperatures (< 50–60 °C), precluding considering these lithofacies

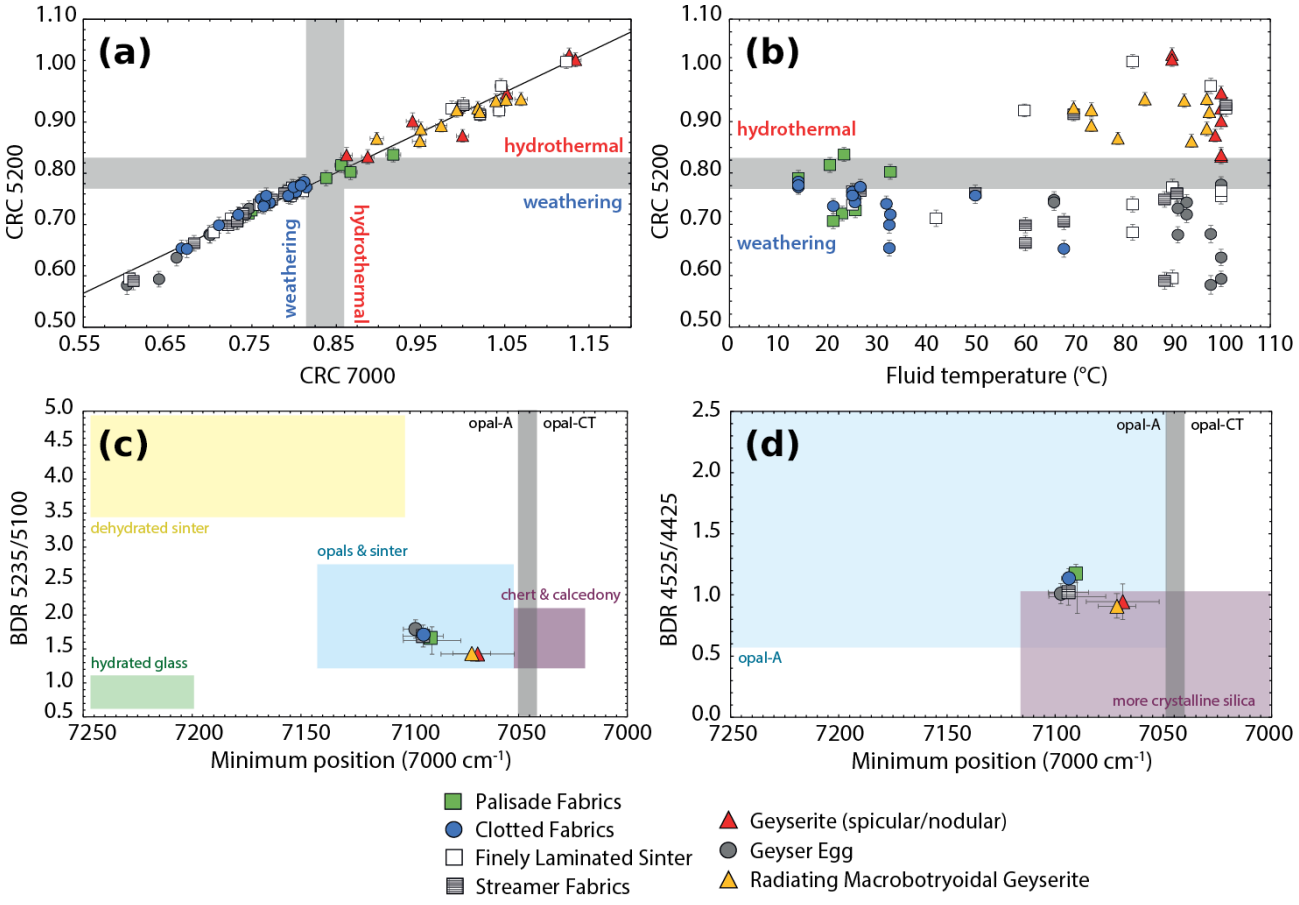

Figure 11. Diagrams illustrating the variations of near-infrared spectral properties according to the lithofacies. **(a)** Plot of the CRC_{5200} versus CRC_{7000} concavity criteria (hydrothermal and weathering fields defined by Chauviré et al., 2017). For this, all 77 individual points are reported to show the very good correlation between the two CRC values. All points are also reported in panel **(b)**. For **(c)** and **(d)** the mean values for each lithofacies are plotted. On all diagrams, the error bars are twice the standard deviation value. **(b)** Plot of the CRC 5200 versus the temperature of the hydrothermal fluid. **(c)** Plot of the 7000 cm^{-1} band minimum position versus the 5235/5100 cm^{-1} band–depth ratio. The ranges of different types of silica are from Rice et al. (2013). **(d)** Plot of the 7000 cm^{-1} band minimum position versus the 4525/4425 cm^{-1} band–depth ratio. The ranges of different types of silica are from Sun and Milliken (2018).

as witnesses of a specific hydrothermal environment or a precise range of fluid temperatures.

Two lithofacies are observed only at low temperatures: palisade fabrics and clotted fabrics. The former consists of the most distal silica sinter samples observed in this study, with measured temperatures below 35 °C. The calculated CRC values on the palisade fabrics samples do not assign them to a high-temperature hydrothermal origin. This is consistent with their geological context of formation closer to ambient temperatures. These samples form far away from hot-spring vents, which makes them less likely to be in constant contact with high-temperature hydrothermal fluids. Therefore, they are more likely to be affected by atmospheric agents such as snow, rain, and subsequent runoff, at ambient temperature. Similar observations and hypotheses can be made for the clotted fabrics samples. These last samples are however observed over a temperature range (10–65 °C) larger than palisade fabrics. Low temperatures of formation could promote the formation of non-indurated, uncemented and porous silica sinter or even cryogenic silica. Indeed, the SEM observations show that clotted fabrics samples are mainly composed of uncemented rounded rod-shaped silica and shard-shaped silica with a significant porosity (Fig. 6d, e). A high porosity could allow a greater surface of contact with atmospheric agents and therefore promote the formation of newly formed silica in thermal equilibrium with the atmosphere. Shard-shaped silica textures are suggested by several authors as evidence of cryogenic silica, i.e., silica that forms at freezing or near-freezing temperatures (Channing and Butler, 2007; Jones and Renaut, 2010; Fox-Powell et al., 2018; Hogancamp et al., 2019). This corroborates the low CRC values that are calculated for these samples. At higher temperatures (50–60 °C), clotted fabrics could be considered newly formed opal that has not been cemented yet. It is also possible

to argue that they form in an environment where the inputs of hydrothermal fluids are not constant or where fluids have started to cool down as they form in a runoff regime. This would, again, favor the circulation of colder waters within the porosity of these juvenile sinters and thus the precipitation of a low- to mid-temperature silica.

In the area close to the hot-spring vents, three lithofacies can be divided into two major clusters by considering the relationships between measured temperatures and the observed spectral properties. The first cluster contains the geyserite and radiating macrobotryoidal geyserite classes. They are sampled in the hot-spring vent area and thus associated with in situ temperatures > 60–90 °C, temperatures considered hydrothermal (Pirajno, 2009). The calculated spectral criteria for these lithofacies give the highest CRC values. These deposits are continuously in contact with (occasionally bubbling) hot fluids and experience little exchanges with the atmosphere. This context contrasts with the conditions of formation of the second cluster represented by the geyser eggs. Although the latter are formed geographically in the same area (not more than one meter away), they exhibit distinct spectral properties. This can be explained by their specific formation mechanism that is closely related to the geyser splash zone dynamics. Surprisingly, these samples exhibit CRC values which are among the lowest of the present sample set. They unambiguously fall in the weathering opal field, despite their high temperature of formation. In this sense, although the morphological characteristics of geyser eggs are unique to hot springs silica sinters, their spectral properties make them an exception in this typically hydrothermal zone.

4.2.2 Microtexture and porosity

The degree of cementation/induration and the consequent porosity of a given sample impact its NIR signature (Christy, 2008). Indeed, the microscopic observations reveal strong texture and structure variations: from one sample to another and even within a single sample at the scale of a few tens to hundreds of micrometers (Fig. 6a, b). Different sequences of precipitation under different physicochemical fluid conditions over time could induce variations in the silanol formation and in the incorporation of the water molecules between the silica spheres. Different water flow regimes (e.g., turbulent versus laminar, constant versus sporadic, splash regime zone) could also have a significant effect on the way silica precipitates. Moreover, porosity is observed in different shapes: pores between uncemented silica spheres, holes or hollows, space between non-contiguous laminae, cracks, or fractures, etc. (Figs. 4c, 6). The porosity can be homogenous or heterogeneous at different scales in the same sample, and the pores can be connected or not to others (e.g. Fig. 4c). Finally, the circulation of fluids is also affected by the type of porosity present in the silica sinter, which then influences the cementation and the early diagenesis of the silica sinter. The great variability of cementation among the samples could be responsible for strong variations of the NIR properties within a single lithofacies. The narrower variability first observed in Chauviré et al. (2017a) could be explained by the used samples that mostly consist of opal samples with homogeneous massive texture (e.g., weathering gem opal fields of Australia or Ethiopia, hydrothermal gem opal fields of Mexico).

4.2.3 Biological features

The abundance of living and silicified organisms in hydrothermal silica sinters has been intensively studied (e.g., Walter and Des Marais, 1993; Jones et al., 2001; Thorolfsdottir and Marteinsson, 2013; Campbell et al., 2015; Guido et al., 2019). Many studies show the good preservation of organic matter, micro-organisms, and macro-organisms in the silica sinters (Jones et al., 1997; Jones and Renaut, 2003a; Geptner et al., 2005; Preston et al., 2008; Guido and Campbell, 2014; Jones and Peng, 2015; Smythe et al., 2016; Fox-Powell et al., 2018; Gong et al., 2020; Teece et al., 2020). However, despite a multitude of studies focused on hot-spring-related life, the effects and roles of biologic activity on silica precipitation and maturation remain poorly constrained and debated. The question remains open of the passive or active roles of microorganisms in the formation of silica sinter (e.g., Jones et al., 1997; Guidry and Chafetz, 2003; Konhauser et al., 2004; Handley et al., 2005; Tobler et al., 2008; Orange et al., 2013; Gong et al., 2020; Sriaporn et al., 2020).

Several studies highlight that the presence of biology in geyserite and sinters has a strong influence on the microtextures, structures, and porosity of silica (e.g., Jones et al., 1997; Jones and Renaut, 2003b; Konhauser et al., 2004; Handley et al., 2005; Boudreau and Lynne, 2012; Orange et al., 2013; Jones and Peng, 2015; Hamilton et al., 2019; Gong et al., 2020; Sriaporn et al., 2020; Jones and Renaut, 2021). The samples presented here show a great diversity of textures, structures, and biological population, which implies that the samples are classified in distinct lithofacies. The precise identification of the biological structures and their relationship with the various silica microfacies are not discussed in the present study. Nevertheless, interactions between silica polymerization and biological activity, implications in terms of structure and porosity, and links with near-infrared properties would benefit future studies. Yet, the contribution of this work on those questions is that, with the current dataset, no correlation between the abundance of biological features and the NIR properties is observed.

4.3 Implications for planetary geology

Surface-reaching hydrothermal systems such as hot springs are prime targets to search for extraterrestrial life. The orbital identification of silica sinter deposits in the solar system requires the validation of geomorphological and mineralogical criteria. The study of the spectral properties of these deposits could provide better constraints on the nature of the

silica and define its geological origin in the case of ambiguous geomorphological context. At the surface of Mars, the opaline silica-rich deposits of the Nili Patera caldera, around the Nili Tholus cone (Syrtis Major Volcanic Province), represent one of the most striking examples of presumed hot-spring-like deposits in the solar system observed from the orbit (Skok et al., 2010; Pineau et al., 2020). Based on NIR remote sensing analyses and the use of spectral criteria (band minima positions and CRC values), Pineau et al. (2020) questioned the hydrothermal origin deciphered solely from the spectroscopic criteria calculations and geomorphology. They obtained CRC values that are close to CRC values of terrestrial opals from weathering origin ($CRC_{5200} < 0.80$). However, the geological context and the geomorphological observations indicate almost unambiguously that the Nili Patera silica deposits formed through hydrothermal activity (Skok et al., 2010; Pineau et al., 2020). To explain this apparent discrepancy, Pineau et al. (2020) proposed two hypotheses: (i) the Nili Patera silica formed through low-temperature hydrothermal activity, or (ii) this silica experienced a high rate of dehydration; both hypotheses potentially explain the low CRC values. The present study shows that some terrestrial silica sinter samples exhibit low CRC values, in the range of terrestrial weathering opals, when they form from low-temperature hydrothermal fluids ($T < 50$–$60\,^{\circ}C$). Thus, although the Nili Patera silica may have spectral properties indicative of increased dehydration, their spectra may also indicate a low-temperature hydrothermal origin. This underlines the importance to combine geomorphological observations with spectral measurements when attempting to ascribe a geological origin to an object, both on Earth and on extraterrestrial bodies.

5 Conclusions

Based on field and microscopic observations, silica sinter samples from Icelandic hot springs were classified into seven distinct lithofacies. The spectral characteristics of their 4500, 5200, and 7000 cm^{-1} (2.2, 1.9 and 1.4 µm respectively) near-infrared absorptions bands were consistent with opal-A (also confirmed by Raman spectroscopy and XRD).

The concavity ratio criteria (CRC) values indicate that only the lithofacies in the near-vent area (geyserite and radiating macrobotryoidal geyserite) fall in the expected hydrothermal spectral field. All the other lithofacies (including geyser eggs, which are located close to geyser vents) fall in the weathering spectral field. Moreover, there is no unambiguous correlation between the NIR signature of silica and the temperature of formation alone.

In addition to temperature, the size and distribution of porosity proved to affect the infrared properties, as well as the degree of silica spheres cementation and the abundance of microbiological activity. Determining the respective influence of these parameters on their NIR properties still requires deeper investigation. At this stage, we propose that there is a link between the NIR signature of silica sinters and their exact environment of formation: both abiogenic parameters (temperature, fluids dynamics) and biogenic parameters (i.e., microbial communities, etc.) control the structure of silica and hence its NIR properties.

In the context of the geological investigation of fossil systems on Earth or extraterrestrial bodies (e.g., Mars), only measurements of high CRC values ($CRC_{5200} > 0.85$; $CRC_{7000} > 0.90$) indicate a hydrothermal origin, when measurements of low CRC values ($CRC_{5200} < 0.75$; $CRC_{7000} < 0.80$) indicate either a continental weathering origin or a low-temperature hydrothermal origin ($T\,^{\circ}C < 50$–$60\,^{\circ}C$).

Data availability. The data that support the findings of this study are available from the corresponding author upon reasonable request or as Supplement related to this article.

Supplement. The supplement related to this article is available online at: https://doi.org/10.5194/ejm-35-949-2023-supplement.

Author contributions. MP: conceptualization; methodology; investigation, resources; writing – original; draft; visualization. BC: conceptualization; methodology; resources; writing – review and editing; visualization. BR: conceptualization; investigation; resources; writing – review and editing; supervision; funding acquisition.

Competing interests. The contact author has declared that none of the authors has any competing interests.

Disclaimer. Publisher's note: Copernicus Publications remains neutral with regard to jurisdictional claims made in the text, published maps, institutional affiliations, or any other geographical representation in this paper. While Copernicus Publications makes every effort to include appropriate place names, the final responsibility lies with the authors.

Acknowledgements. We thank Brian Grégoire and Fabien Baron (IC2MP, UMR-CNRS-7285, Université de Poitiers, France) for their help with and advice on NIR analysis of the powdered samples. Laurent Lenta (LPG, UMR-CNRS-6112, Nantes Université, France) helped in the preparation of polished sections. Nicolas Stephant and Pierre-Emmanuel Petit (IMN, UMR-CNRS-6502, Nantes Université, France) contributed to the acquisition of the scanning electron microscope and X-ray diffraction data. Sami Soudani (LPG, UMR-CNRS-6112, Nantes Université, France) conducted preliminary measurements. We thank the editor, Roland Stalder, and the two reviewers, Ayrton Hamilton and one anonymous referee, for their remarks and suggestions for improving the manuscript.

Financial support. This research has been supported by the Agence Nationale de la Recherche (ANR, France) under the two contracts: (i) grant no. ANR-16-CE31-0012 entitled Mars-Prime and (ii) grant no. ANR-20-CE49-0013 entitled PaleoSilica and the Centre national de la Recherche Scientifique (CNRS, France). This work also benefited from the support of EuroPlanet 22020 RI that received funding from the European Union's Horizon 2020 research and innovation program under grant no. 654208. This work was also supported by the Programme National de Planétologie (PNP, France) of CNRS/INSU, co-funded by the Centre National d'Études Spatiales (CNES, France). The authors also received financial support from the European Union (ERDF) and Région Nouvelle Aquitaine.

Review statement. This paper was edited by Roland Stalder and reviewed by Ayrton Hamilton and one anonymous referee.

References

Anderson, J. H. and Wickersheim, K. A.: Near infrared characterization of water and hydroxyl groups on silica surfaces, Surf. Sci., 2, 252–260, https://doi.org/10.1016/0039-6028(64)90064-0, 1964.

Barghoorn, E. S. and Tyler, S. A.: Microorganisms from the Gunflint Chert, Science, 147, 563–575, https://doi.org/10.1126/science.147.3658.563, 1965.

Bell, P. R., Fanti, F., Hart, L. J., Milan, L. A., Craven, S. J., Brougham, T., and Smith, E.: Revised geology, age, and vertebrate diversity of the dinosaur-bearing Griman Creek Formation (Cenomanian), Lightning Ridge, New South Wales, Australia, Palaeogeogr. Palaeocl., 514, 655–671, https://doi.org/10.1016/j.palaeo.2018.11.020, 2019.

Boboň, M., Christy, A. A., Kluvanec, D., and Illášová, L.: State of water molecules and silanol groups in opal minerals: A near infrared spectroscopic study of opals from Slovakia, Phys. Chem. Miner., 38, 809–818, https://doi.org/10.1007/s00269-011-0453-0, 2011.

Boudreau, A. E. and Lynne, B. Y.: The growth of siliceous sinter deposits around high-temperature eruptive hot springs, J. Volcanol. Geoth. Res., 247/248, 1–8, https://doi.org/10.1016/j.jvolgeores.2012.07.008, 2012.

Cady, S. L., Skok, J. R., Gulick, V. G., Berger, J. A., and Hinman, N. W.: Siliceous Hot Spring Deposits: Why They Remain Key Astrobiological Targets, Elsevier Inc., 179–210, https://doi.org/10.1016/b978-0-12-809935-3.00007-4, 2018.

Campbell, K. A., Guido, D. M., Gautret, P., Foucher, F., Ramboz, C., and Westall, F.: Geyserite in hot-spring siliceous sinter: Window on Earth's hottest terrestrial (paleo)environment and its extreme life, Earth Sci. Rev., 148, 44–64, https://doi.org/10.1016/j.earscirev.2015.05.009, 2015.

Carter, J., Riu, L., Poulet, F., Bibring, J.-P., Langevin, Y., and Gondet, B.: A Mars orbital catalog of aqueous alteration signatures (MOCAAS), Icarus, 389, 115164, https://doi.org/10.1016/j.icarus.2022.115164, 2023.

Channing, A. and Butler, I. B.: Cryogenic opal-A deposition from Yellowstone hot springs, Earth Planet. Sc. Lett., 257, 121–131, https://doi.org/10.1016/j.epsl.2007.02.026, 2007.

Chauviré, B. and Thomas, P. S.: DSC of natural opal: insights into the incorporation of crystallisable water in the opal microstructure, J. Therm. Anal. Calorim., 140, 2077–2085, https://doi.org/10.1007/s10973-019-08949-4, 2020.

Chauviré, B., Rondeau, B., and Mangold, N.: Near infrared signature of opal and chalcedony as a proxy for their structure and formation conditions, Europ. J. Mineral., 29, 409–421, https://doi.org/10.1127/ejm/2017/0029-2614, 2017a.

Chauviré, B., Rondeau, B., Mazzero, F., and Ayalew, D.: The precious opal deposit at Wegel Tena, Ethiopia: Formation via successive pedogenesis events, Can. Mineral., 55, 701–723, https://doi.org/10.3749/canmin.1700010, 2017b.

Chauviré, B., Houadria, M., Donini, A., Berger, B. T., Rondeau, B., Kritsky, G., and Lhuissier, P.: Arthropod entombment in weathering-formed opal: new horizons for recording life in rocks, Sci. Rep., 10, 10575, https://doi.org/10.1038/s41598-020-67412-9, 2020.

Chauviré, B., Pineau, M., Quirico, E., and Beck, P.: Near infrared signature of opaline silica at Mars-relevant pressure and temperature, Earth Planet. Sc. Lett., 576, 117239, https://doi.org/10.1016/j.epsl.2021.117239, 2021.

Choblet, G., Tobie, G., Buch, A., Čadek, O., Barge, L. M., Bēhounková, M., Camprubi, E., Freissinet, C., Hedman, M., Jones, G., Lainey, V., Le Gall, A., Lucchetti, A., MacKenzie, S., Mitri, G., Neveu, M., Nimmo, F., Olsson-Francis, K., Panning, M., Postberg, F., Saur, J., Schmidt, J., Sekine, Y., Shibuya, T., Sotin, C., Soucek, O., Szopa, C., Usui, T., Vance, S., and Van Hoolst, T.: Enceladus as a potential oasis for life: Science goals and investigations for future explorations, Exp. Astron., 54, 809–847, https://doi.org/10.1007/s10686-021-09808-7, 2021.

Christy, A. A.: Quantitative determination of surface area of silica gel particles by near infrared spectroscopy and chemometrics, Colloid Surface A, 322, 248–252, https://doi.org/10.1016/j.colsurfa.2008.03.021, 2008.

Christy, A. A.: Near infrared spectroscopic characterisation of surface hydroxyl groups on hydrothermally treated silica gel, Int. J. Chem. Environ. Eng., 2, 27–32, 2011.

Damer, B. and Deamer, D.: The hot spring hypothesis for an origin of life, Astrobiology, 20, 429–452, https://doi.org/10.1089/ast.2019.2045, 2020.

Day, R. and Jones, B.: Variations in Water Content in Opal-A and Opal-CT from Geyser Discharge Aprons, J. Sediment. Res., 78, 301–315, https://doi.org/10.2110/jsr.2008.030, 2008.

Djokic, T., Van Kranendonk, M. J., Campbell, K. A., Walter, M. R., and Ward, C. R.: Earliest signs of life on land preserved in ca. 3.5 Ga hot spring deposits, Nat. Commun., 8, 16149, https://doi.org/10.1038/ncomms16149, 2017.

Fox-Powell, M. G., Channing, A., Applin, D., Cloutis, E., Preston, L. J., and Cousins, C. R.: Cryogenic silicification of microorganisms in hydrothermal fluids, Earth Planet. Sc. Lett., 498, 1–8, https://doi.org/10.1016/j.epsl.2018.06.026, 2018.

Gaillou, E., Fritsch, E., Aguilar-Reyes, B., Rondeau, B., Post, J., Barreau, A., and Ostroumov, M.: Common gem opal: An investigation of micro- to nano-structure, Am. Mineral., 93, 1865–1873, https://doi.org/10.2138/am.2008.2518, 2008.

Galeener, F. L.: Planar rings in glasses, Solid State Commun., 44, 1037–1040, https://doi.org/10.1016/0038-1098(82)90329-5, 1982a.

Galeener, F. L.: Planar rings in vitreous silica, J. Non. Cryst. Solids, 49, 53–62, https://doi.org/10.1016/0022-3093(82)90108-9, 1982b.

Geptner, A. R., Ivanovskaya, T. A., and Pokrovskaya, E. V.: Hydrothermal fossilization of microorganisms at the Earth's Surface in Iceland, Lithol. Mineral Res., 40, 505–520, https://doi.org/10.1007/s10987-005-0048-2, 2005.

Gong, J., Myers, K. D., Munoz-Saez, C., Homann, M., Rouillard, J., Wirth, R., Schreiber, A., and Van Zuilen, M. A.: Formation and preservation of microbial palisade fabric in silica deposits from El tatio, Chile, Astrobiology, 20, 500–524, https://doi.org/10.1089/ast.2019.2025, 2020.

Guido, D. M. and Campbell, K. A.: A large and complete Jurassic geothermal field at Claudia, Deseado Massif, Santa Cruz, Argentina, J. Volcanol. Geotherm. Res., 275, 61–70, https://doi.org/10.1016/j.jvolgeores.2014.02.013, 2014.

Guido, D. M., Campbell, K. A., Foucher, F., and Westall, F.: Life is everywhere in sinters: Examples from jurassic hot-spring environments of argentine patagonia, Geol. Mag., 156, 1631–1638, https://doi.org/10.1017/S0016756819000815, 2019.

Guidry, S. A. and Chafetz, H. S.: Anatomy of siliceous hot springs: Examples from Yellowstone National Park, Wyoming, USA, Sediment Geol., 157, 71–106, https://doi.org/10.1016/S0037-0738(02)00195-1, 2003.

Hamilton, A. R., Campbell, K. A., and Guido, D. M.: Atlas of Siliceous Hot Spring Deposits (Sinter) and other Silicified Surface Manifestations in Epithermal Environments, edited by: Lower Hutt, N. Z., GNS Science, GNS Science report 2019/06, 56 pp., https://doi.org/10.21420/BQDR-XQ16, 2019.

Handley, K. M., Campbell, K. A., Mountain, B. W., and Browne, P. R. L.: Abiotic-biotic controls on the origin and development of spicular sinter: In situ growth experiments, Champagne Pool, Waiotapu, New Zealand, Geobiology, 3, 93–114, https://doi.org/10.1111/j.1472-4669.2005.00046.x, 2005.

Herdianita, N. R., Browne, P. R. L., Rodgers, K. A., and Campbell, K. A.: Mineralogical and textural changes accompanying ageing of silica sinter, Miner Depos, 35, 48–62, https://doi.org/10.1007/s001260050005, 2000.

Herrmann, J. R., Maas, R., Rey, P. F., and Best, S. P.: The nature and origin of pigments in black opal from Lightning Ridge, New South Wales, Australia, Aust. J. Earth Sci., 66, 1027–1039, https://doi.org/10.1080/08120099.2019.1587643, 2019.

Hogancamp, J. V., Lapen, T. J., Chafetz, H. S., and Elsenousy, A.: The effect of solution chemistries and freezing temperatures on the morphology of cryogenic opal-A (COA): Implications for past climates on Mars, Chem. Geol., 519, 56–67, https://doi.org/10.1016/j.chemgeo.2019.04.017, 2019.

Hsu, H.-W., Postberg, F., Sekine, Y., Shibuya, T., Kempf, S., Horányi, M., Juhász, A., Altobelli, N., Suzuki, K., Masaki, Y., Kuwatani, T., Tachibana, S., Sirono, S., Moragas-Klostermeyer, G., and Srama, R.: Ongoing hydrothermal activities within Enceladus, Nature, 519, 207–210, https://doi.org/10.1038/nature14262, 2015.

Jones, B.: Siliceous sinters in thermal spring systems: Review of their mineralogy, diagenesis, and fabrics, Sediment Geol., 413, 105820, https://doi.org/10.1016/j.sedgeo.2020.105820, 2021.

Jones, B. and Peng, X.: Laminae development in opal-A precipitates associated with seasonal growth of the form-genus Calothrix (Cyanobacteria), Rehai geothermal area, Tengchong, Yunnan Province, China, Sediment Geol., 319, 52–68, https://doi.org/10.1016/j.sedgeo.2015.01.004, 2015.

Jones, B. and Renaut, R. W.: Hot spring and geyser sinters: the integrated product of precipitation, replacement, and deposition, Can. J. Earth Sci., 40, 1549–1569, https://doi.org/10.1139/e03-078, 2003a.

Jones, B. and Renaut, R. W.: Petrography and genesis of spicular and columnar geyserite from the Whakarewarewa and Orakeikorako geothermal areas, North Island, New Zealand, Can. J. Earth Sci., 40, 1585–1610, https://doi.org/10.1139/e03-062, 2003b.

Jones, B. and Renaut, R. W.: Microstructural changes accompanying the opal-A to opal-CT transition: New evidence from the siliceous sinters of Geysir, Haukadalur, Iceland, Sedimentology, 54, 921–948, https://doi.org/10.1111/j.1365-3091.2007.00866.x, 2007.

Jones, B. and Renaut, R. W.: Impact of seasonal changes on the formation and accumulation of soft siliceous sediments on the discharge apron of geysir, Iceland, J. Sediment. Res., 80, 17–35, https://doi.org/10.2110/jsr.2010.008, 2010.

Jones, B. and Renaut, R. W.: Multifaceted incremental growth of a geyser discharge apron – Evidence from Geysir, Haukadalur, Iceland, Sediment Geol., 419, 105905, https://doi.org/10.1016/j.sedgeo.2021.105905, 2021.

Jones, B., Renaut, R. W., and Rosen, M. R.: Biogenicity of silica precipitation around geysers and hot-spring vents, North Island, New Zealand, J. Sediment. Res., 67, 88–104, https://doi.org/10.1306/d42684ff-2b26-11d7-8648000102c1865d, 1997.

Jones, B., Renaut, R. W., and Rosen, M. R.: Taphonomy of Silicified Filamentous Microbes in Modern Geothermal Sinters: Implications for Identification, Palaios, 16, 580–592, https://doi.org/10.2307/3515630, 2001.

Jones, J. B. and Segnit, E. R.: The nature of opal I. nomenclature and constituent phases, J. Geol. Soc. Austr., 18, 57–67, https://doi.org/10.1080/00167617108728743, 1971.

Kastner, M., Keene, J. B., and Gieskes, J. M.: Diagenesis of siliceous oozes – I. Chemical controls on the rate of opal-A to opal-CT transformation – an experimental study, Geochim. Cosmochim. Ac., 41, 1041–1059, https://doi.org/10.1016/0016-7037(77)90099-0, 1977.

Kelley, D. S., Baross, J. A., and Delaney, J. R.: Volcanoes, fluids, and life at mid-ocean ridge spreading centers, Annu. Rev. Earth Planet. Sci., 30, 385–491, https://doi.org/10.1146/annurev.earth.30.091201.141331, 2002.

Konhauser, K. O., Jones, B., Phoenix, V. R., Ferris, G., and Renaut, R. W.: The microbial role in hot spring silicification, Ambio, 33, 552–558, https://doi.org/10.1579/0044-7447-33.8.552, 2004.

Langer, K. and Florke, O. W.: Near infrared absorption spectra (4000–9000 cm^{-1}) of opals and the role of "water" in these $SiO_2 \cdot nH_2O$ minerals, Fortschritte der Mineralogie, 52, 17–51, 1974.

Liesegang, M. and Gee, C. T.: Silica entry and accumulation in standing trees in a hot-spring environment: cellular pathways, rapid pace and fossilization potential, Palaeontology, 63, 651–660, https://doi.org/10.1111/pala.12480, 2020.

Lynne, B. Y., Campbell, K. A., Moore, J. N., and Browne, P. R. L.: Diagenesis of 1900-year-old siliceous sinter (opal-A to quartz) at Opal Mound, Roosevelt Hot

Springs, Utah, USA, Sediment Geol., 179, 249–278, https://doi.org/10.1016/j.sedgeo.2005.05.012, 2005.

Lynne, B. Y., Campbell, K. A., James, B. J., Browne, P. R. J., and Moore, J.: Tracking crystallinity in siliceous hot-spring deposits, Am. J. Sci., 307, 612–641, https://doi.org/10.2475/03.2007.03, 2007.

Des Marais, D. J. and Walter, M. R.: Terrestrial Hot Spring Systems: Introduction, Astrobiology, 19, 1419–1432, https://doi.org/10.1089/ast.2018.1976, 2019.

Milliken, R. E., Swayze, G. A., Arvidson, R. E., Bishop, J. L., Clark, R. N., Ehlmann, B. L., Green, R. O., Grotzinger, J. P., Morris, R. V., Murchie, S. L., Mustard, J. F., and Weitz, C.: Opaline silica in young deposits on Mars, Geology, 36, 847–850, https://doi.org/10.1130/G24967A.1, 2008.

Morris, R. V, Vaniman, D. T., Blake, D. F., Gellert, R., Chipera, S. J., Rampe, E. B., Ming, D. W., Morrison, S. M., Downs, R. T., Treiman, A. H., Yen, A. S., Grotzinger, J. P., Achilles, C. N., Bristow, T. F., Crisp, J. A., Des Marais, D. J., Farmer, J. D., Fendrich, K. V, Frydenvang, J., Graff, T. G., Morookian, J.-M., Stolper, E. M., and Schwenzer, S. P.: Silicic volcanism on Mars evidenced by tridymite in high-SiO_2 sedimentary rock at Gale crater, P. Natl. Acad. Sci. USA, 113, 7071–7076, https://doi.org/10.1073/pnas.1607098113, 2016.

Orange, F., Lalonde, S. V., and Konhauser, K. O.: Experimental simulation of evaporation-driven silica sinter formation and microbial silicification in hot spring systems, Astrobiology, 13, 163–176, https://doi.org/10.1089/ast.2012.0887, 2013.

Ostrooumov, M., Fritsch, E., Lasnier, B., and Lefrant, S.: Spectres Raman des opales: aspect diagnostique et aide à la classification, European J. Mineral., 11, 899–908, 1999.

Pan, L., Carter, J., Quantin-Nataf, C., Pineau, M., Chauviré, B., Mangold, N., Le Deit, L., Rondeau, B., and Chevrier, V.: Voluminous Silica Precipitated from Martian Waters during Late-stage Aqueous Alteration, Planet Sci. J., 2, 23 pp., https://doi.org/10.3847/PSJ/abe541, 2021.

Phillips, J. C.: Microscopic origin of anomalously narrow Raman lines in network glasses, J. Non. Cryst. Solids, 63, 347–355, https://doi.org/10.1016/0022-3093(84)90102-9, 1984.

Pineau, M., Le Deit, L., Chauviré, B., Carter, J., Rondeau, B., and Mangold, N.: Toward the geological significance of hydrated silica detected by near infrared spectroscopy on Mars based on terrestrial reference samples, Icarus, 347, 113706, https://doi.org/10.1016/j.icarus.2020.113706, 2020.

Pirajno, F.: Hydrothermal processes and Mineral Systems, Springer N., Springer Netherlands, 1250 pp., https://doi.org/10.1007/978-1-4020-8613-7, 2009.

Preston, L. J., Benedix, G. K., Genge, M. J., and Sephton, M. A.: A multidisciplinary study of silica sinter deposits with applications to silica identification and detection of fossil life on Mars, Icarus, 198, 331–350, https://doi.org/10.1016/j.icarus.2008.08.006, 2008.

Rice, M. S., Cloutis, E. A., Bell, J. F., Bish, D. L., Horgan, B. H., Mertzman, S. A., Craig, M. A., Renaut, R. W., Gautason, B., and Mountain, B.: Reflectance spectra diversity of silica-rich materials: Sensitivity to environment and implications for detections on Mars, Icarus, 223, 499–533, https://doi.org/10.1016/j.icarus.2012.09.021, 2013.

Rodgers, K. A., Browne, P. R. L., Buddle, T. F., Cook, K. L., Greatrex, R. A., Hampton, W. A., Herdianita, N. R., Holland, G. R., Lynne, B. Y., Martin, R., Newton, Z., Pastars, D., Sannazarro, K. L., and Teece, C. I. A.: Silica phases in sinters and residues from geothermal fields of New Zealand, Earth Sci. Rev., 66, 1–61, https://doi.org/10.1016/j.earscirev.2003.10.001, 2004.

Rondeau, B., Cenki-Tok, B., Fritsch, E., Mazzero, F., Gauthier, J.-P. J.-P., Bodeur, Y., Bekele, E., Gaillou, E., and Ayalew, D.: Geochemical and petrological characterization of gem opals from Wegel Tena, Wollo, Ethiopia: opal formation in an Oligocene soil, Geochemistry: Exploration, Environ., Anal., 12, 93–104, https://doi.org/10.1144/1467-7873/10-MINDEP-058, 2012.

Ruff, S. W., Farmer, J. D., Calvin, W. M., Herkenhoff, K. E., Johnson, J. R., Morris, R. V., Rice, M. S., Arvidson, R. E., Bell, J. F., Christensen, P. R., and Squyres, S. W.: Characteristics, distribution, origin, and significance of opaline silica observed by the Spirit rover in Gusev crater, Mars, J. Geophys. Res. E, 116, E00F23, https://doi.org/10.1029/2010JE003767, 2011.

Ruff, S. W., Campbell, K. A., Van Kranendonk, M. J., Rice, M. S., and Farmer, J. D.: The case for ancient hot springs in gusev crater, mars, Astrobiology, 20, 475–499, https://doi.org/10.1089/ast.2019.2044, 2019.

Skok, J. R., Mustard, J. F., Ehlmann, B. L., Milliken, R. E., and Murchie, S. L.: Silica deposits in the Nili Patera caldera on the Syrtis Major volcanic complex on Mars, Nat. Geosci., 3, 838–841, https://doi.org/10.1038/ngeo990, 2010.

Smallwood, A. G., Thomas, P. S., and Ray, A. S.: Characterisation of sedimentary opals by Fourier transform Raman spectroscopy, Spectrochim. Acta A, 53, 2341–2345, https://doi.org/10.1016/S1386-1425(97)00174-1, 1997.

Smythe, W. F., McAllister, S. M., Hager, K. W., Hager, K. R., Tebo, B. M., and Moyer, C. L.: Silica biomineralization of Calothrix-dominated biofacies from Queen's Laundry hot-spring, Yellowstone National Park, USA, Front. Environ. Sci., 4, 1–11, https://doi.org/10.3389/fenvs.2016.00040, 2016.

Squyres, S. W., Arvidson, R. E., Ruff, S., Gellert, R., Morris, R. V., Ming, D. W., Crumpler, L., Farmer, J. D., Marais, D. J. D., Yen, A., McLennan, S. M., Calvin, W., Bell, J. F., Clark, B. C., Wang, A., McCoy, T. J., Schmidt, M. E., and de Souza, P. A.: Detection of Silica-Rich Deposits on Mars, Science, 320, 1063–1067, https://doi.org/10.1126/science.1155429, 2008.

Sriaporn, C., Campbell, K. A., Millan, M., Ruff, S. W., Van Kranendonk, M. J., and Handley, K. M.: Stromatolitic digitate sinters form under wide-ranging physicochemical conditions with diverse hot spring microbial communities, Geobiology, 18, 619–640, https://doi.org/10.1111/gbi.12395, 2020.

Sun, V. Z. and Milliken, R. E.: Distinct Geologic Settings of Opal-A and More Crystalline Hydrated Silica on Mars, Geophys. Res. Lett., 45, 10221–10228, https://doi.org/10.1029/2018GL078494, 2018.

Teece, B. L., George, S. C., Djokic, T., Campbell, K. A., Ruff, S. W., and Van Kranendonk, M. J.: Biomolecules from fossilized hot spring sinters: Implications for the search for life on mars, Astrobiology, 20, 537–551, https://doi.org/10.1089/ast.2018.2018, 2020.

Thomas, P. S., Guerbois, J.-P., and Smallwood, A. G.: Low temperature DSC characterisation of water in opal, J. Therm. Anal. Calorim., 113, 1255–1260, https://doi.org/10.1007/s10973-012-2911-4, 2013.

Thorolfsdottir, B. O. T. and Marteinsson, V. T.: Microbiological analysis in three diverse natural geothermal bathing pools

in Iceland, Int. J. Environ. Res. Publ. Hlth., 10, 1085–1099, https://doi.org/10.3390/ijerph10031085, 2013.

Tobler, D. J., Stefánsson, A., and Benning, L. G.: In-situ grown silica sinters in Icelandic geothermal areas, Geobiology, 6, 481–502, https://doi.org/10.1111/j.1472-4669.2008.00179.x, 2008.

Torfason, H.: Jarðhitarannsóknir á Hveravöllum 1996, Geothermal research at Hveravellir, Orkustofnun, ISBN: 9979827947, http://www.os.is/gogn/Skyrslur/OS-1997/OS-97025.pdf (last access: 10 March 2023), 1997.

van den Heuvel, D. B., Gunnlaugsson, E., and Benning, L. G.: Surface roughness affects early stages of silica scale formation more strongly than chemical and structural properties of the substrate, Geothermics, 87, 101835, https://doi.org/10.1016/j.geothermics.2020.101835, 2020.

Walter, M. R.: Chapter 3.3 Geyserites of Yellowstone National Park: An Example of Abiogenic "Stromatolites", Develop. Sediment., 20, 87–112, https://doi.org/10.1016/S0070-4571(08)71131-2, 1976.

Walter, M. R. and Des Marais, D. J.: Preservation of biological information in thermal spring deposits: developing a strategy for the search for fossil life on Mars, Icarus, 101, 129–143, https://doi.org/10.1006/icar.1993.1011, 1993.